

Bayesian Prompt Flow Learning for Zero-Shot Anomaly Detection

Zhen Qu^{1,2} Xian Tao^{1,2,4}✉ Xinyi Gong³ Shichen Qu^{1,2} Qiyu Chen^{1,2}
 Zhengtao Zhang^{1,2,4} Xingang Wang^{1,2,5} Guiguang Ding⁶

¹Institute of Automation, Chinese Academy of Sciences

²School of Artificial Intelligence, University of Chinese Academy of Sciences ³HDU

⁴Casivision ⁵Luoyang Institute for Robot and Intelligent Equipment ⁶Tsinghua University

{quzhen2022, xiantao2013, qushichen2023, chenqiyu2021, xingang.wang, zhengtao.zhang}@ia.ac.cn

gongxinyi@hdu.edu.cn dinggg@tsinghua.edu.cn

Abstract

Recently, vision-language models (e.g. CLIP) have demonstrated remarkable performance in zero-shot anomaly detection (ZSAD). By leveraging auxiliary data during training, these models can directly perform cross-category anomaly detection on target datasets, such as detecting defects on industrial product surfaces or identifying tumors in organ tissues. Existing approaches typically construct text prompts through either manual design or the optimization of learnable prompt vectors. However, these methods face several challenges: 1) handcrafted prompts require extensive expert knowledge and trial-and-error; 2) single-form learnable prompts struggle to capture complex anomaly semantics; and 3) an unconstrained prompt space limits generalization to unseen categories. To address these issues, we propose Bayesian Prompt Flow Learning (Bayes-PFL), which models the prompt space as a learnable probability distribution from a Bayesian perspective. Specifically, a prompt flow module is designed to learn both image-specific and image-agnostic distributions, which are jointly utilized to regularize the text prompt space and improve the model’s generalization on unseen categories. These learned distributions are then sampled to generate diverse text prompts, effectively covering the prompt space. Additionally, a residual cross-modal attention (RCA) module is introduced to better align dynamic text embeddings with fine-grained image features. Extensive experiments on 15 industrial and medical datasets demonstrate our method’s superior performance. The code is available at <https://github.com/xiaozhen228/Bayes-PFL>.

1. Introduction

In the fields of industrial defect detection [18, 32, 41, 42] and medical image analysis [2, 8, 11, 29], the cold-start

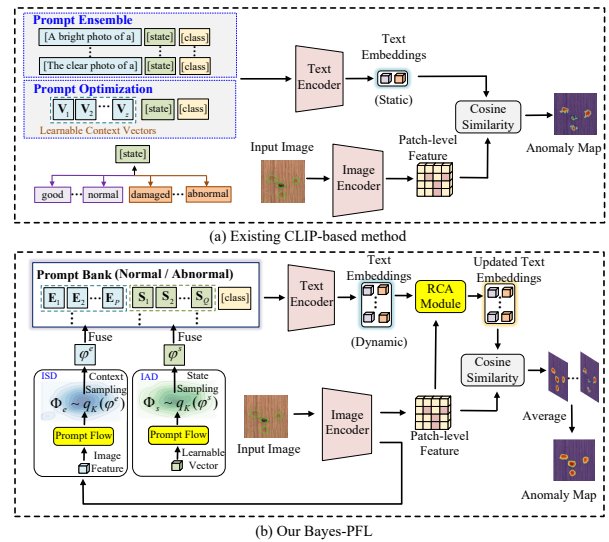


Figure 1. Comparison of existing CLIP-based method and our Bayes-PFL. Our Bayes-PFL learns the distributions of context and state words within textual prompts. The proposed RCA module is further to enhance the alignment between dynamic text embeddings and patch-level features through cross-modal interaction.

problem is a major challenge, characterized by an insufficient amount of labeled data for supervised training on new object categories. An effective solution is zero-shot anomaly detection (ZSAD), which directly detects anomalies on new object surface after being trained on auxiliary data. However, significant variations in background features, anomaly types, and visual appearances across different products and organs make it difficult to achieve robust generalization.

Vision-language models (VLMs), such as CLIP [34] and ALIGN [20], which are trained on large-scale image-text pairs through contrastive representation learning, have shown significant potential for ZSAD. As a representa-

tive VLM, CLIP [34] has been widely adopted in previous works [8, 18, 49]. A key challenge for CLIP-based ZSAD methods is the effective design of text prompts. As illustrated in Figure 1(a), a typical textual prompt consists of three components: *context words*, *state words*, and *class*. They respectively represent a general description of the object (e.g. background), the attributes indicating whether it is normal or anomalous (e.g. good / damaged), and the object category (e.g. wood). Existing text prompt design methods can be broadly categorized into two types: prompt ensemble-based and prompt optimization-based. Prompt ensemble-based methods, such as WinCLIP [18], APRIL-GAN [9], and CLIP-AD [10], create hand-crafted prompt templates and embed various context and state words into these templates to generate a large number of textual prompts. However, the number of context and state words is limited and the design relies on expert knowledge. In contrast, prompt optimization-based methods, such as AnomalyCLIP [49] and AdaCLIP [8], replace the context words in the prompts with learnable vectors or directly insert them into the encoder. However, two critical issues are often overlooked: 1) The design of learnable prompts is overly simplistic, which makes it difficult to capture complex context semantics; 2) The learnable prompt space is not properly constrained, hindering the generalization of learnable text prompts to unseen categories.

To address these challenges, we propose a Bayesian Prompt Flow Learning (Bayes-PFL) strategy based on CLIP for the ZSAD task. As depicted in Figure 1(b), our approach learns a probability distribution over textual prompts from a Bayesian inference perspective, aiming to improve the ZSAD performance through two key aspects: 1) regularizing the context and state text spaces separately through the design of image-specific distribution (ISD) and image-agnostic distribution (IAD), ensuring that the learned prompts generalize effectively to novel categories, and 2) enhancing the coverage of the prompt space by sampling prompts from the learned probability distribution.

First, we construct two-class prompt banks to store learnable textual prompts for normal and abnormal cases. Then, a prompt flow module is designed to learn the distribution of context and state words within the text prompts. Specifically, to introduce rich visual semantics into the text prompts, ISD is learned through prompt flow to model the context words, dynamically adapting based on the input image. To encode unified normal and abnormal semantics, IAD is established for the state words, remaining static and conditioned on a learnable free vector. Finally, multiple textual prompts sampled from the learned distribution are fused with the prompt banks to generate enriched text prompts. Moreover, to align the sampled text embeddings with fine-grained image features, we introduce a residual cross-modal attention (RCA) module to enhance the inter-

action between modalities. Unlike existing methods [8–10] that directly align text with patch-level features as shown in Figure 1(a), our RCA module updates dynamic text embeddings using fine-grained image information to improve the ZSAD performance. The results generated from alignment of multiple updated text embeddings and patch-level feature are integrated to produce the final anomaly map.

The contributions of this work are summarized as follows: 1) We propose a novel Bayesian Prompt Flow Learning method, Bayes-PFL, built on CLIP to address the ZSAD problem. By distribution sampling and distribution regularization of the text prompt space, Bayes-PFL enhances the ZSAD performance on novel categories; 2) The prompt flow module is designed to learn ISD and IAD, which model the context and state semantics in text prompts, respectively. Additionally, the RCA module is introduced to improve the alignment between fine-grained features and dynamic text prompts through cross-modal interactions; 3) After training on auxiliary datasets, our method can directly detect defects / lesions on novel products / organs without requiring target training data. Extensive experiments across 15 industrial and medical datasets demonstrate that Bayes-PFL achieves state-of-the-art (SOTA) performance in ZSAD.

2. Related Works

2.1. Zero-shot Anomaly Detection

The earliest work, WinCLIP [18], proposes a window-based strategy to aggregate classification results obtained from aligning text with sub-images at multiple scales. APRIL-GAN [9] and CLIP-AD [10] use trainable adapter layers to map fine-grained patch features into a joint embedding space. The latter further employs feature surgery to mitigate opposite predictions. Additionally, several existing studies have integrated multiple foundation models, such as SAM [25] and GroundingDINO [28], to collectively enhance ZSAD performance, as demonstrated in SAA/SAA+ [7] and ClipSAM [27]. Recently, an increasing number of prompt optimization-based methods have been proposed. AnomalyCLIP [49] and Filo [13] insert learnable vectors into the input text or CLIP encoder layers to avoid extensive engineering on hand-crafted prompt design. AdaCLIP [8] and VCP-CLIP [33] further utilize textual and visual hybrid prompts to enhance CLIP’s anomaly perception capability. Different from these methods, our Bayes-PFL learns the distribution of textual prompts and leverages sampling to cover the prompt space to improve the ZSAD performance.

2.2. Prompt Design

The design of textual prompts plays a pivotal role in applying VLMs to downstream tasks. Manually crafted textual prompts [15, 26, 34, 43, 45] and data-driven approaches to obtain learnable prompts [14, 35, 44, 47, 48] in the natural

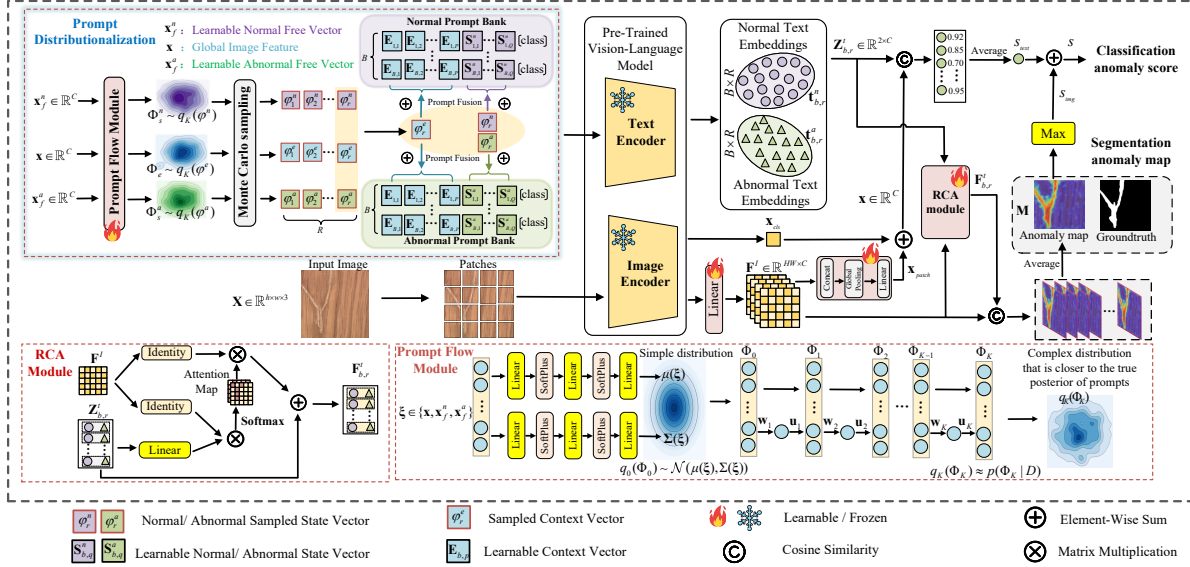


Figure 2. The framework of Bayes-PFL. First, a prompt bank with B sets of learnable prompts is constructed (Section 3.2). Next, the prompt flow module converts the learnable prompts into a probabilistic distribution and generates $B \times R$ text embeddings through R rounds of sampling (Sections 3.3 and 3.4), which are then aligned with image and patch features (Section 3.5).

scenario have both demonstrated effectiveness in zero-shot learning. In the ZSAD task, Compositional Prompt Ensemble [9, 10, 18] and Prompt Optimization [8, 33, 49] are two mainstream methods for text prompt design.

Compositional Prompt Ensemble generates diverse text prompts through the combination of state words and textual templates. In the representative work APRIL-GAN [9], approximately 35 templates and 5 state words are designed for abnormal descriptions, resulting in a total of 35×5 text prompts. The text embeddings from these prompts are averaged to produce the final result, and a similar approach is applied to normal descriptions.

Prompt Optimization replaces the context words in text prompts with learnable vectors or directly inserts these vectors into the encoder layers. As depicted in Figure 1(a), the representative method AnomalyCLIP [49] designs text prompts in the form of $[\mathbf{V}_1][\mathbf{V}_2] \cdots [\mathbf{V}_z][\text{state}][\text{object}]$, where $\mathbf{V}_i, i = 1, 2, \dots, z$ are learnable vectors. However, the single-form prompt design and the lack of effective constraints on the prompt space limit its generalization capability to unseen categories.

3. Method

Our approach follows the recent ZSAD task setting, where the model is trained in a supervised manner on seen categories C^s from an industrial dataset and then directly tested on unseen categories C^u from other industrial or medical datasets. Notably, $C^u \cap C^s = \emptyset$, and the object categories used for auxiliary training and testing come from different

datasets with large domain gaps.

3.1. Overview

Figure 2 illustrates the main framework of Bayes-PFL, which consists of three key designs: 1) Two-class prompt banks for normal and abnormal textual descriptions, 2) A prompt flow module for distribution learning, and 3) A RCA module for feature alignment. Given an input image $\mathbf{X} \in \mathbb{R}^{h \times w \times 3}$, the model first maps the patch-level image features to the joint embedding space through a single linear layer, producing $\mathbf{F}^I \in \mathbb{R}^{HW \times C}$, where $H = h/\text{patchsize}$, $W = w/\text{patchsize}$ and C represents the dimensionality of the joint embedding space. Subsequently, the prompt flow module learns the image-specific distribution $q_K(\varphi^e)$ for context words, and the image-agnostic distributions $q_K(\varphi^n)$, $q_K(\varphi^a)$ for normal and abnormal state words. Monte Carlo sampling [1] is applied to these distributions, and the sampled results φ_r^e , φ_r^n , φ_r^a are fused with the prompt banks to generate diverse textual prompts. The text embeddings $\mathbf{Z}_{b,r}^t$ are aligned with \mathbf{F}^I to obtain multiple anomaly segmentation results, which are averaged to derive the final anomaly map \mathbf{M} . Note that when aligning with \mathbf{F}^I , we additionally employ the proposed RCA module to refine the text embeddings to $\mathbf{F}_{b,r}^t$.

3.2. Two-class Prompt Banks

We decompose the text prompt into three components: context words, state words, and class words. Unlike previous prompt optimization strategies [49], which manually design state words and only optimize context words, we argue that

state words (e.g., good / damaged) still reside within an optimizable prompt space. Thus, in the word embedding space, the manually designed context and state words are replaced with learnable vectors. Inspired by Compositional Prompt Ensemble, normal and abnormal prompt banks are further constructed to expand the prompt space, with each containing B distinct trainable prompts:

$$g_b^n = [\mathbf{E}_{b,1}][\mathbf{E}_{b,2}] \cdots [\mathbf{E}_{b,P}][\mathbf{S}_{b,1}^n] \cdots [\mathbf{S}_{b,Q}^n][\text{class}] \quad (1)$$

$$g_b^a = [\mathbf{E}_{b,1}][\mathbf{E}_{b,2}] \cdots [\mathbf{E}_{b,P}][\mathbf{S}_{b,1}^a] \cdots [\mathbf{S}_{b,Q}^a][\text{class}] \quad (2)$$

where $b = 1, 2, \dots, B$. $\mathbf{E}_{b,i} \in \mathbb{R}^C, i = 1, 2, \dots, P$ are learnable vectors designed to encode contextual information in the text. $\mathbf{S}_{b,j}^n, \mathbf{S}_{b,j}^a \in \mathbb{R}^C, j = 1, 2, \dots, Q$ are learnable normal and abnormal state vectors, respectively. Note that we enforce orthogonality among the text embeddings generated from the same prompt bank, promoting diversity in the normal or anomalous semantics captured by different prompts. This constraint is implemented through the orthogonal loss \mathcal{L}_{ort} introduced in Section 3.6.

3.3. Prompt Distributionalization

Prompt distributionalization expresses a process of modeling and generating rich textual prompts by utilizing the prompt flow module, and fusing the sampled results from the distribution with the prompt banks. This process not only enhances the model’s generalization to unseen categories by constraining the prompt space to ISD and IAD (distribution regularization), but also comprehensively covers the prompt space through distribution sampling.

Bayesian inference. Assume the auxiliary training dataset is $D = \{\mathbf{X}, Y_c, \mathbf{Y}_s\}$, where $\mathbf{X} \in \mathbb{R}^{h \times w \times 3}$ represents the input image, and $Y_c \in \{0, 1\}$, $\mathbf{Y}_s \in \mathbb{R}^{h \times w}$ denote the image-level labels and pixel-level ground truth, respectively. To construct the text prompt distribution, the context, normal state, and abnormal state word embeddings are represented as C -dimensional random vectors Φ_e, Φ_s^n and Φ_s^a , respectively. For convenience, we denote $\Phi = \{\Phi_e, \Phi_s^n, \Phi_s^a\}$. The posterior probabilities are then computed as:

$$p(\Phi|D) = \frac{p(D|\Phi)p(\Phi)}{p(D)} \quad (3)$$

Since computing the marginal likelihood $p(D)$ is intractable, variational inference [21] with distribution $q_\gamma(\Phi)$, parameterized by γ , is employed to approximate the posterior probability. Note that our method operates under the mean-field assumption, where all variables are mutually independent: $q_\gamma(\Phi) = q_\gamma(\varphi^e)q_\gamma(\varphi^n)q_\gamma(\varphi^a)$. By applying Jensen’s inequality, an upper bound is driven for the log marginal likelihood of the training data:

$$\log p(D) = \log \int p(D|\Phi)p(\Phi)d\Phi \quad (4)$$

$$\geq E_{q_\gamma(\Phi|D)}[\log p(D, \Phi) - \log q_\gamma(\Phi|D)] = -\mathcal{L}_e(D) \quad (5)$$

Thus, the variational distribution $q_\gamma(\Phi)$ can be obtained by minimizing the evidence lower bound (ELBO) loss $\mathcal{L}_e(D)$.

Prompt flow module. Richer posterior approximations enable us to better estimate the prompt distribution [36]. Hence, a prompt flow module is designed to transform a simple probability distribution $q_0(\Phi_0)$ into a more complex one $q_K(\Phi_K)$ through a series of invertible mappings $h_k, k = 1, 2, \dots, K$. Specifically, this transformation follows $\Phi_K = h_K(h_{K-1}(\cdots h_1(\Phi_0)))$, as illustrated in the bottom right corner of Figure 2. For the model efficiency, we use a linear-time transformation $h(\Phi) = \Phi + \mathbf{u}g(\mathbf{w}^T\Phi + \mathbf{b})$, where $\mathbf{w}, \mathbf{u} \in \mathbb{R}^C, \mathbf{b} \in \mathbb{R}$ are trainable parameters and $g(\cdot)$ is the *Tanh* activation function [38]. After K transformations, the final distribution is given by:

$$\log q_K(\Phi_K) = \log q_0(\Phi_0) - \sum_{k=1}^K \log |1 + \mathbf{u}_k^T \phi(\Phi_k)| \quad (6)$$

where $\phi(\Phi) = g'(\mathbf{w}^T\Phi + \mathbf{b})\mathbf{w}$. By replacing $q_\gamma(\Phi|D)$ in Equation (5) with $q_K(\Phi_K)$, the objective function for optimizing the prompt flow module is computed as:

$$\begin{aligned} \mathcal{L}_p(D) &= E_{q_\gamma(\Phi|D)}[\log q_\gamma(\Phi|D) - \log p(D, \Phi)] \\ &= E_{q_0(\Phi_0)} \left[\log q_0(\Phi_0) - \sum_{k=1}^K \log |1 + \mathbf{u}_k^T \phi(\Phi_k)| \right] \\ &\quad - E_{q_0(\Phi_0)}[\log p(\Phi_K)] - E_{q_0(\Phi_0)}[\log p(D|\Phi_K)] \quad (7) \end{aligned}$$

where the prior distribution follows $p = \mathcal{N}(0, \mathbf{I})$. The initial density q_0 is defined as a standard normal distribution: $q_0 = \mathcal{N}(\boldsymbol{\mu}(\boldsymbol{\xi}), \boldsymbol{\Sigma}(\boldsymbol{\xi}))$, where $\boldsymbol{\mu} \in \mathbb{R}^C$ and $\text{diag}(\boldsymbol{\Sigma}) = \boldsymbol{\sigma} \in \mathbb{R}^C$ are conditioned on the vector $\boldsymbol{\xi} \in \mathbb{R}^C$ and parameterized by three linear layers, with a Softplus activation function [38] applied between consecutive layers.

Depending on the different inputs $\boldsymbol{\xi}$ to the prompt flow module, two types of distributions are obtained: an **image-specific distribution** (ISD) and an **image-agnostic distribution** (IAD). For ISD, $\boldsymbol{\xi}$ is set as global image feature \mathbf{x} to acquire a dynamic distribution, which models the context distribution and enhances generalization in unseen domains. For IAD, we set $\boldsymbol{\xi}$ as the learnable free vectors \mathbf{x}_f^n and \mathbf{x}_f^a , respectively, while sharing the same network weights. This static distribution is used to learn a unified state semantics for both normal and abnormal conditions.

Prompt sampling and fusion. Monte Carlo sampling is used to sample R iterations from the initial densities q_0^e, q_0^n, q_0^a . The sampled results are processed through the prompt flow module to obtain $\varphi_r^e, \varphi_r^n, \varphi_r^a, r = 1, 2, \dots, R$, which represent sampled context vector, normal sampled state vector and abnormal sampled state vector, respectively. The fusion process is formulated as:

$$g_{b,r}^n = [\mathbf{E}_{b,1} + \varphi_r^e][\mathbf{E}_{b,2} + \varphi_r^e] \cdots [\mathbf{E}_{b,P} + \varphi_r^e] [\mathbf{S}_{b,1}^n + \varphi_r^n] \cdots [\mathbf{S}_{b,Q}^n + \varphi_r^n][\text{class}] \quad (8)$$

$$g_{b,r}^a = [\mathbf{E}_{b,1} + \varphi_r^e][\mathbf{E}_{b,2} + \varphi_r^e] \cdots [\mathbf{E}_{b,P} + \varphi_r^e] \quad (9)$$

$$[\mathbf{S}_{b,1}^a + \varphi_r^a] \cdots [\mathbf{S}_{b,Q}^a + \varphi_r^a][\text{class}]$$

where $g_{b,r}^n$, $g_{b,r}^a$ represent the text prompt obtained from the r -th sampling of the b -th prompt in the prompt banks, respectively. After sampling and fusion, the number of prompts in each bank increases to $B \times R$ at a very low cost. Note that to ensure proper gradient backpropagation after discrete sampling, the reparameterization method [23] is employed during the optimization process.

3.4. Residual Cross-modal Attention Module

The normal and abnormal text embeddings, derived from the text prompts in Equations (8) and (9) through the text encoder, are represented as $\mathbf{t}_{b,r}^n$ and $\mathbf{t}_{b,r}^a$, respectively. Due to the design of image-specific distribution and Monte Carlo sampling, the generated text embeddings are dynamic during both training and inference. This presents challenges in aligning text embeddings $\mathbf{Z}_{b,r}^t \in \mathbb{R}^{2 \times C}$ with fine-grained patch embeddings $\mathbf{F}^I \in \mathbb{R}^{H \times W \times C}$ in anomaly segmentation task, where $\mathbf{Z}_{b,r}^t$ is the concatenation of $\mathbf{t}_{b,r}^n$ and $\mathbf{t}_{b,r}^a$ along the sequence dimension. Therefore, the RCA module is designed to promote cross-modal interaction between textual and fine-grained image features, which can be formulated as follows:

$$\mathbf{F}_{b,r}^t = \mathbf{Z}_{b,r}^t + \text{softmax}(\mathbf{Q}_{b,r}(\mathbf{F}^I)^T / \sqrt{C})\mathbf{F}^I \quad (10)$$

where $\mathbf{F}_{b,r}^t \in \mathbb{R}^{2 \times C}$ is the refined text embeddings. The query embedding $\mathbf{Q}_{b,r} = \mathbf{Z}_{b,r}^t \mathbf{W}$, where $\mathbf{W} \in \mathbb{R}^{C \times C}$ is the weight matrix of a linear mapping layer. The RCA module introduces residuals to: 1) fuse original textual features with cross-modal features for better zero-shot performance and 2) facilitate gradient backpropagation to the prompt bank, improving the optimization of learnable prompts.

3.5. Anomaly Map and Anomaly Score

Pixel-level anomaly map. We extract L -layer patch-level features \mathbf{F}_l^I and align them with the refined text embeddings $\mathbf{F}_{l,b,r}^t$, $l = 1, 2, \dots, L$. The anomaly map from the l -th layer is computed as:

$$\mathbf{M}_{l,b,r} = \text{softmax}(Up(\widetilde{\mathbf{F}}_l^I \widetilde{\mathbf{F}}_{l,b,r}^{tT})) \quad (11)$$

where $\widetilde{(\cdot)}$ denotes the L_2 -normalization operation along the embedding dimension and $Up(\cdot)$ is the unsampling operation. The final result $\mathbf{M} \in \mathbb{R}^{h \times w}$ is obtained by averaging the anomaly maps derived from aligning the L -layer patch features with $B \times R$ refined text embeddings:

$$\mathbf{M} = \frac{1}{LBR} \sum_{l=1}^L \sum_{b=1}^B \sum_{r=1}^R \mathbf{M}_{l,b,r} \quad (12)$$

Image-level anomaly score. For anomaly classification, the anomaly values come from both the text and image branches. The anomaly score in the text branch is computed as: $s_{text} = (\frac{1}{BR}) \sum_b \sum_r \text{softmax}(\widetilde{\mathbf{x}} \widetilde{\mathbf{Z}}_{b,r}^{tT})$, where $\mathbf{x} = \mathbf{x}_{cls} + \mathbf{x}_{patch}$ is the global image embedding. Note that \mathbf{x}_{cls} refers to the global image features obtained from the class token of the vanilla image encoder, while \mathbf{x}_{patch} comes from the fusion of fine-grained patch features. Specifically, the patch features $\mathbf{F}_l^I \in \mathbb{R}^{H \times W \times C}$, $l = 1, 2, \dots, L$ from different layers are first concatenated along the channel dimension. Then, global average pooling is applied along the spatial dimensions, followed by a linear layer that maps the results to \mathbf{x}_{patch} . The anomaly score from the image branch is derived from the maximum value of the anomaly map: $s_{img} = \max(\mathbf{M})$. The final image-level anomaly score is then expressed as: $s = s_{text} + s_{img}$.

3.6. Loss Function

During the training stage, a single Monte Carlo sampling is performed to enhance efficiency. Let the text prompts from B samples be denoted as $[g_{b,1}^n, g_{b,1}^a]$, $b \in \{1, 2, \dots, B\}$, and their corresponding text embeddings as $[\mathbf{t}_{b,1}^n, \mathbf{t}_{b,1}^a]$, $b \in \{1, 2, \dots, B\}$. To enhance the diversity of learnable prompts in prompt banks, an orthogonal loss is designed on the text embeddings as follows:

$$\mathcal{L}_{ort} = \sum_{i=1}^B \sum_{j=1, j \neq i}^B \{(\langle \mathbf{t}_{i,1}^n, \mathbf{t}_{j,1}^n \rangle)^2 + (\langle \mathbf{t}_{i,1}^a, \mathbf{t}_{j,1}^a \rangle)^2\} \quad (13)$$

in which $\langle \cdot, \cdot \rangle$ denotes the cosine similarity. The final loss function can be expressed as:

$$\mathcal{L} = \mathcal{L}_{ort} + \mathcal{L}_p \quad (14)$$

where the prompt flow loss \mathcal{L}_p is computed using Equation (7). The first two terms of \mathcal{L}_p are distribution regularization terms that refine the initial distribution $q_0(\Phi_0)$ into a simple prior $p(\Phi_K)$, effectively controlling the distribution of latent variables. This regularization ensures that the prompt flow module can learn an effective prompt distribution, mitigating overfitting while enhancing the generalization of the prompts. The third term, $E_{q_0(\Phi_0)}[\log p(D|\Phi_K)]$, maximizes the log-likelihood of the data, which is approximated by the sum of classification loss (for text-image alignment) and segmentation loss (for text-patch alignment). Specifically, our Bayes-PFL employs a cross-entropy loss for classification, along with the sum of Focal loss [37] and Dice loss [30] for segmentation. More details about the loss function can be found in Appendix A.1.

4. Experiments

4.1. Experimental Setup

Datasets. To evaluate the ZSAD performance of the model, experiments on 15 real-world datasets from the industrial

Table 1. Comparison with existing state-of-the-art methods. The best results are marked in red, while the second-best are indicated in blue.

Domain	Metric	Dataset	WinCLIP [18]	APRIL-GAN [9]	CLIP-AD [10]	AnomalyCLIP [49]	AdaCLIP [8]	Bayes-PFL
Industrial	Image-level (AUROC, F1-Max, AP)	MVTec-AD	(91.8, 92.9 , 95.1)	(86.1, 90.4, 93.5)	(89.8, 91.1, 95.3)	(91.5, 92.8, 96.2)	(92.0, 92.7, 96.4)	(92.3, 93.1, 96.7)
		VisA	(78.1, 79.0, 77.5)	(78.0, 78.7, 81.4)	(79.8, 79.2, 84.3)	(82.1, 80.4, 85.4)	(83.0, 81.6, 84.9)	(87.0, 84.1, 89.2)
		BTAD	(83.3, 81.0, 84.1)	(74.2, 70.0, 71.7)	(85.8, 81.7, 85.2)	(89.1, 86.0, 91.1)	(91.6, 88.9, 92.4)	(93.2, 91.9, 96.5)
		KSDD2	(93.5, 71.4, 77.9)	(90.3, 70.0, 74.4)	(95.2, 84.4, 88.2)	(92.1, 71.0, 77.8)	(95.9, 84.5, 95.9)	(97.3, 92.3, 97.9)
		RSDD	(85.3, 73.5, 65.3)	(73.1, 59.7, 50.5)	(88.3, 74.1, 73.9)	(73.5, 59.0, 55.0)	(89.1, 75.0 , 70.8)	(94.1, 89.6, 92.3)
		DAGM	(89.6, 86.4, 90.4)	(90.4, 86.9, 90.1)	(90.8, 88.4, 90.5)	(95.6, 93.2, 94.6)	(96.5, 94.1, 95.7)	(97.7, 95.7, 97.0)
Industrial	Pixel-level (AUROC, PRO, AP)	DTD-Synthetic	(95.0, 94.3, 97.9)	(83.9, 89.4, 93.6)	(91.5, 91.8, 96.8)	(94.5, 94.5 , 97.7)	(92.8, 92.2, 97.0)	(95.1, 95.1, 98.4)
		MVTec-AD	(85.1, 64.6, 18.0)	(87.6, 44.0, 40.8)	(89.8, 70.6, 40.0)	(91.1, 81.4, 34.5)	(86.8, 33.8, 38.1)	(91.8, 87.4, 48.3)
		VisA	(79.6, 56.8, 5.0)	(94.2, 86.8, 25.7)	(95.0, 86.9, 26.3)	(95.5, 87.0, 21.3)	(95.1, 71.3, 29.2)	(95.6, 88.9, 29.8)
		BTAD	(71.4, 32.8, 11.2)	(91.3, 23.0, 32.9)	(93.1, 59.8, 46.7)	(93.3, 69.3, 42.0)	(87.7, 17.1, 36.6)	(93.9, 76.6, 47.1)
		KSDD2	(97.9, 91.2, 17.1)	(97.9, 51.1, 61.6)	(99.3, 85.4, 58.9)	(99.4, 92.7, 41.8)	(96.1, 70.8, 56.4)	(99.6, 97.6, 73.7)
		RSDD	(95.1, 75.4, 2.1)	(99.4, 64.9, 30.6)	(99.2, 90.1, 31.9)	(99.1, 92.0, 19.1)	(99.5, 50.5, 38.2)	(99.6, 98.0, 39.1)
Medical	Image-level (AUROC, F1-Max, AP)	DAGM	(83.2, 55.4, 3.1)	(99.2, 44.7, 42.6)	(99.0, 83.1, 40.7)	(99.1, 93.6, 29.5)	(97.0, 40.9, 44.2)	(99.3, 98.0, 43.1)
		DTD-Synthetic	(82.5, 55.4, 11.6)	(96.6, 41.6, 67.3)	(97.1, 68.7, 62.3)	(97.6, 88.3, 52.4)	(94.1, 24.9, 52.8)	(97.8, 94.3, 69.9)
		HeadCT	(83.7, 78.8, 81.6)	(89.3, 82.0, 89.6)	(93.8, 90.5 , 92.2)	(95.3, 89.7, 95.2)	(93.4, 86.5, 92.2)	(96.5, 92.9, 95.5)
		BrainMRI	(92.0, 84.2, 90.7)	(89.6, 85.3, 84.5)	(92.8, 88.7, 85.5)	(96.1, 92.3, 92.3)	(94.9, 90.4, 94.2)	(96.2, 92.8, 92.4)
		Br35H	(80.5, 74.1, 82.2)	(93.1, 85.4, 92.9)	(96.0, 90.8, 95.5)	(97.3, 92.4, 96.1)	(95.7, 89.1, 95.7)	(97.8, 93.6, 96.2)
		Medical	Pixel-level (AUROC, PRO, AP)	ISIC	(83.3, 55.1, 62.4)	(85.8, 13.7, 69.8)	(81.6, 29.0, 65.5)	(88.4, 78.1, 74.4)
CVC-ColonDB	(64.8, 28.4, 14.3)			(78.4, 28.0, 23.2)	(80.3, 58.8, 23.7)	(81.9, 71.4, 31.3)	(79.3, 6.5, 26.2)	(82.1, 76.1, 31.9)
CVC-ClinicDB	(70.7, 32.5, 19.4)			(86.0, 41.2, 38.8)	(85.8, 69.7 , 39.0)	(85.9, 69.6, 42.2)	(84.3, 14.6, 36.0)	(89.6, 78.4, 53.2)
Endo	(68.2, 28.3, 23.8)			(84.1, 32.3, 47.9)	(85.6, 57.0, 51.7)	(86.3, 67.3, 50.4)	(84.0, 10.5, 44.8)	(89.2, 74.8, 58.6)
Medical	Pixel-level (AUROC, PRO, AP)	Kvasir	(69.8, 31.0, 27.5)	(80.2, 27.1, 42.4)	(82.5, 48.1, 46.2)	(81.8, 53.8, 42.5)	(79.4, 12.3, 43.8)	(85.4, 63.9, 54.2)

and medical domains are conducted. Specifically, we utilize seven commonly used industrial anomaly detection datasets, including MVTEC-AD [4], VisA [50], BTAD [31], KSDD2 [6], RSDD [46], DAGM [12] and DTD-Synthetic [3]. Eight different datasets in the medical domain are used, including HeadCT [39], BrainMRI [22], and Br35H [16] for brain tumor classification, CVC-ColonDB [40], CVC-ClinicDB [5], Endo [17], and Kvasir [19] for colon polyp segmentation and ISIC [11] for skin cancer detection. Following [10, 33], we perform auxiliary training on one industrial dataset and directly infer on other industrial and medical datasets. Since the categories in VisA do not overlap with those in the other datasets, we use VisA as the auxiliary training set. To assess VisA itself, we fine-tune our model on the MVTEC-AD dataset. More details about the datasets can be found in Appendix C.

Evaluation Metrics. For classification, we report image-level metrics: Area Under the Receiver Operating Characteristic (AUROC), the maximum F1 score at the optimal threshold (F1-Max) and the average precision (AP). For segmentation, pixel-level AUROC, AP and Per-Region Overlap (PRO) are employed to evaluate the model’s ability.

Implementation Details. The publicly available CLIP (*ViT-L-14-336*) pretrained by OpenAI [34] is adopted in this study. Following previous works [8, 9, 49], we standardize the resolution of input images to 518×518 and select the 6th, 12th, 18th, 24th layers from the 24-layer image encoder to extract patch embeddings. The number of prompts B in the prompt banks is set to 3 and flow length K is set to 10 by default. The length of learnable context vectors P and learnable state vectors Q are both set to 5. During the auxiliary training and inference stages, the number of Monte Carlo sampling iterations R is set to 1 and 10, respectively. We use the Adam [24] optimizer to train our Bayes-PFL for

a total of 20 epochs, with an initial learning rate of 0.0001 and a batch size of 32. All experiments are conducted on a single NVIDIA 3090 GPU, with 5 random seeds selected. The experimental results are the averages of different object categories from the target dataset. More implementation details can be found in Appendix A.1.

4.2. Comparison with State-of-the-art methods

In this study, five SOTA methods are employed for comparison with our Bayes-PFL, including WinCLIP [18], APRIL-GAN [9], CLIP-AD [10], AnomalyCLIP [49], and AdaCLIP [8]. To ensure a fair comparison, we use the same backbone, input image resolution, and experimental settings (training on VisA and testing on other datasets) for all methods. More details regarding the comparison of these methods are shown in Appendix A.2.

Quantitative Comparison. Table 1 presents the quantitative results of ZSAD across different datasets in both industrial and medical domains. Our Bayes-PFL achieves state-of-the-art performance on image-level and pixel-level metrics across nearly all datasets in comparison with other methods. For example, on the medical dataset ISIC, our Bayes-PFL outperforms the second-best approach by 3.8%, 9.5%, and 10.2% in pixel-level AUROC, PRO, and AP, respectively. The poor PRO performance of AdaCLIP is attributed to the high variance in its predicted anomaly scores and its limited ability to effectively detect large anomalous regions. In contrast, Bayes-PFL explores a broader prompt space by sampling from the distribution, enhancing the detection of large anomalous regions. Note that the anomaly detection results on the medical dataset are directly derived from the fine-tuned weights of the industrial dataset VisA, indicating that the feature spaces for anomalies in these two domains overlap to some extent.

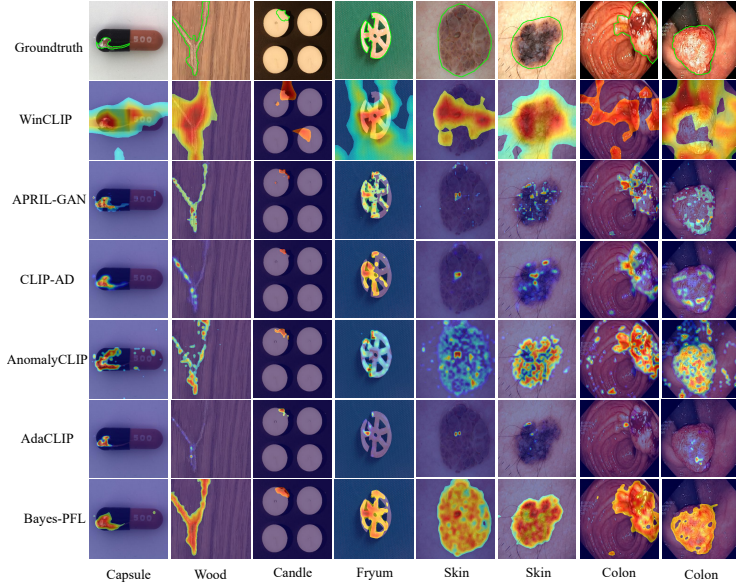


Figure 3. Qualitative comparison of anomaly segmentation results across different ZSAD methods. The images in the first four columns are from the industrial datasets MVTec-AD [4], VisA [50], whereas those in the last four columns are from the medical datasets ISIC [11], Kvasir [19], and CVC-ClinicDB [5].

Qualitative Comparison. Figure 3 visualizes anomaly maps from both industrial and medical datasets. It can be observed that our Bayes-PFL achieves more accurate segmentation results and more complete anomaly region localization compared to other methods. Especially in categories from the medical domain (e.g., colon, skin), our method demonstrates a significant advantage. These results indicate that the learned prompt distribution can cover a more comprehensive prompt space and capture the anomaly semantics in images from different novel categories.

Performance comparison at different training epochs. In Figure 4, we compare APRIL-GAN [9] and AnomalyCLIP [49], which employ two different text prompt design strategies, with our Bayes-PFL across various training epochs. The pixel-level AP during testing is reported to evaluate ZSAD performance. For a fair comparison, we modify these methods by replacing only their text prompt designs while keeping all other components identical to Bayes-PFL. These modified versions are referred to as APRIL-GAN+ and AnomalyCLIP+, respectively. Our Bayes-PFL achieves stable and consistently improving AP throughout training, surpassing the other two methods and highlighting the advantages of our prompt flow learning approach. In contrast, APRIL-GAN+ and AnomalyCLIP+ exhibit performance declines after reaching their peak AP values, with the latter showing a more significant degradation. In Appendix B.4, we further explore this phenomenon and analyze the reasons behind it.

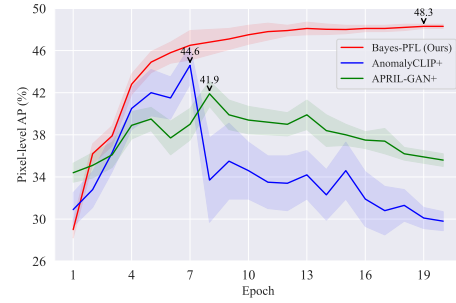


Figure 4. Pixel-level AP during the test stage at different epoches on the MVTec-AD dataset.

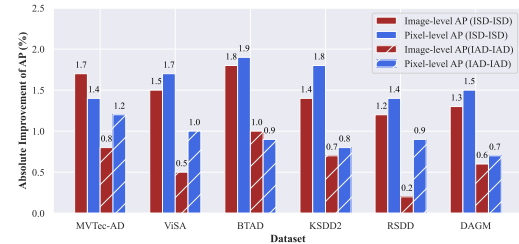


Figure 5. Absolute AP improvement of using our ISD-IAD compared to ISD-ISD and IAD-IAD.

Remark. Our Bayes-PFL outperforms other SOTA approaches for three main reasons: 1) The prompt flow module effectively regularizes the prompt space with ISD and IAD, thereby enhancing the model’s generalization performance on unseen categories; 2) The distribution sampling adaptively generates diverse text prompts to cover the prompt space. The ensemble of results from rich prompts enables better ZSAD performance in Bayes-PFL; 3) The RCA module facilitates cross-modal intersection and enhances the alignment capability of different modalities.

4.3. Image-specific vs. Image-agnostic distribution

In Bayes-PFL, ISD and IAD are modeled in the context and state word embedding spaces, respectively, referred to collectively as ISD-IAD. A natural question arises: why not use ISD-ISD or IAD-IAD instead? In Figure 5, we compare the absolute AP improvement achieved by using ISD-IAD over ISD-ISD and IAD-IAD across six industrial datasets. Higher values indicate a more pronounced advantage of our approach. It can be observed that all metrics are positive, indicating that ISD-IAD outperforms the other two distribution design strategies. This is because the text prompts need to learn unified normal and abnormal semantics across different categories, making the static IAD more suitable for capturing category-invariant state representations. The dynamic ISD incorporates visual features, aiding in the acquisition of rich contextual information (e.g., object background) in the context word embeddings.

Table 2. Ablation on different components.

		Image-level		Pixel-level	
		AUROC	AP	AUROC	AP
Module Ablation	w/o ISD	89.1	94.5	88.3	46.5
	w/o IAD	90.3	95.2	89.5	47.2
	w/o ISD, IAD	88.6	93.3	87.1	45.6
	w/o RCA	91.8	95.9	89.7	46.1
Loss Ablation	w/o \mathcal{L}_{ort}	91.2	96.0	90.2	47.3
Classification Ablation	w/o \mathbf{x}_{cls}	89.3	94.4	—	—
	w/o \mathbf{x}_{patch}	90.9	95.8	—	—
	w/o s_{text}	89.0	95.1	—	—
	w/o s_{img}	90.9	95.3	—	—
Bayes-PFL		92.3	96.7	91.8	48.3

Table 3. Ablation on the number of Monte Carlo sampling iterations during inference. (mean \pm std)

R	Image-level		Pixel-level		Time (ms)
	AUROC	AP	AUROC	AP	
1	89.5 \pm 1.1	94.1 \pm 1.2	87.1 \pm 1.3	45.4 \pm 0.6	132.2 \pm 1.6
3	90.0 \pm 1.0	94.8 \pm 0.9	88.2 \pm 1.2	46.1 \pm 0.6	200.3 \pm 1.4
5	91.1 \pm 0.8	95.4 \pm 0.9	89.5 \pm 1.0	46.8 \pm 0.5	254.2 \pm 1.4
7	92.0 \pm 0.7	96.3 \pm 0.8	90.9 \pm 0.8	47.5 \pm 0.5	297.4 \pm 1.7
10	92.7 \pm 0.4	96.8 \pm 0.5	91.8 \pm 0.6	48.3 \pm 0.4	388.5 \pm 1.5
13	92.7 \pm 0.4	96.9 \pm 0.5	91.9 \pm 0.5	48.4 \pm 0.4	467.5 \pm 1.5
16	92.8 \pm 0.3	96.9 \pm 0.4	92.0 \pm 0.4	48.6 \pm 0.3	621.6 \pm 1.6
20	92.9 \pm 0.2	97.0 \pm 0.2	92.1 \pm 0.2	48.9 \pm 0.1	726.1 \pm 1.7

4.4. Ablation

In this subsection, ablation experiments on the MVTec-AD dataset are conducted to further investigate the impact of different settings on the proposed Bayes-PFL.

Influence of different components. Ablation studies on modules, loss functions, and classifications are conducted separately, as summarized in Table 2. The module ablation study shows that ZSAD performance declines when the RCA module or any distribution type in the prompt flow module is removed. Notably, omitting ISD results in a greater performance drop than omitting IAD in all metrics, indicating that context distribution modeling conditioned on the image has a greater impact on generalization ability. Not using the orthogonal loss \mathcal{L}_{ort} also leads to a decrease of approximately 1% in both image-level and pixel-level metrics. In the classification ablation study, the best performance is achieved when all components are included. This suggests that the results from the text and image branches complement each other, and integrating fine-grained patch features into the global image features \mathbf{x}_{cls} from the vanilla CLIP model helps enhance classification performance.

Influence of the number of sampling iterations. The ZSAD performance on novel categories under different sampling iterations R is presented in Table 3. Additionally, the standard deviation and average inference time per image (calculated from 50 images) are reported to assess the stability of the results and inference efficiency. As the number

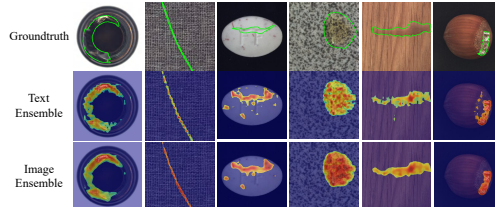


Figure 6. Visualization of different ensemble modes.

Table 4. Ablation on different ensemble mode

Ensemble Mode	Image-level		Pixel-level		Time (ms)
	AUROC	AP	AUROC	AP	
Text Ensemble	92.0	96.3	91.1	47.6	436.6
Image Ensemble	92.3	96.7	91.8	48.3	443.4

of sampling iterations increases, our method demonstrates improved zero-shot generalization performance and stability, but at the cost of longer inference times. Consequently, we identified a trade-off at $R = 10$, which is set as the default value in our experiments. More ablation studies on the hyperparameters can be found in Appendix B.

Influence of the ensemble mode. Given the text embeddings $\mathbf{t}_{b,r}^n$ and $\mathbf{t}_{b,r}^a$, we consider two ensemble modes: 1) Text ensemble, where text embeddings are averaged first and then aligned with image features; and 2) Image ensemble, where image features are aligned separately first, followed by averaging the anomaly scores or maps. Table 4 compares the ZSAD performance of these modes along with the average inference time per image. The results show that image ensemble outperforms text ensemble while maintaining comparable inference efficiency. As illustrated in Figure 6, image ensemble produces more complete detection results with higher confidence in anomalous regions. Therefore, we adopt image ensemble as the default approach for generating the final ZSAD results.

5. Conclusion

This paper presents a novel ZSAD method, Bayes-PFL, which models text prompt spaces as a probabilistic distribution. A prompt flow module generates ISD and IAD to model context and state prompt spaces, capturing prompt uncertainty and enhancing generalization to new categories by regularizing the prompt space. Rich text prompts are generated by combining distribution sampling with prompt banks, improving ZSAD performance through an ensemble approach. Additionally, an RCA module aligns dynamic text embeddings with fine-grained image features. These designs enable Bayes-PFL to achieve state-of-the-art ZSAD performance on 15 publicly available industrial and medical datasets.

Acknowledgement

This work is supported in part by the National Science and Technology Major Project of China under Grant 2022ZD0119402; in part by the National Natural Science Foundation of China under Grant No 62373350 and 62371179; in part by the Youth Innovation Promotion Association CAS (2023145); in part by the Beijing Nova Program 20240484687.

References

- [1] Christophe Andrieu, Nando De Freitas, Arnaud Doucet, and Michael I Jordan. An introduction to mcmc for machine learning. *Machine learning*, 50:5–43, 2003. 3
- [2] Syed Muhammad Anwar, Muhammad Majid, Adnan Qayyum, Muhammad Awais, Majdi Alnowami, and Muhammad Khurram Khan. Medical image analysis using convolutional neural networks: a review. *Journal of medical systems*, 42:1–13, 2018. 1
- [3] Toshimichi Aota, Lloyd Teh Tzer Tong, and Takayuki Okatani. Zero-shot versus many-shot: Unsupervised texture anomaly detection. In *Proceedings of the IEEE/CVF Winter Conference on Applications of Computer Vision*, pages 5564–5572, 2023. 6
- [4] Paul Bergmann, Michael Fauser, David Sattlegger, and Carsten Steger. Mvtec ad—a comprehensive real-world dataset for unsupervised anomaly detection. In *Proceedings of the IEEE/CVF conference on computer vision and pattern recognition*, pages 9592–9600, 2019. 6, 7
- [5] Jorge Bernal, F Javier Sánchez, Gloria Fernández-Esparrach, Debora Gil, Cristina Rodríguez, and Fernando Vilariño. Wm-dova maps for accurate polyp highlighting in colonoscopy: Validation vs. saliency maps from physicians. *Computerized medical imaging and graphics*, 43:99–111, 2015. 6, 7
- [6] Jakob Božič, Domen Tabernik, and Danijel Skočaj. Mixed supervision for surface-defect detection: From weakly to fully supervised learning. *Computers in Industry*, 129: 103459, 2021. 6
- [7] Yunkang Cao, Xiaohao Xu, Chen Sun, Yuqi Cheng, Zongwei Du, Liang Gao, and Weiming Shen. Segment any anomaly without training via hybrid prompt regularization. *arXiv preprint arXiv:2305.10724*, 2023. 2
- [8] Yunkang Cao, Jiangning Zhang, Luca Frittoli, Yuqi Cheng, Weiming Shen, and Giacomo Boracchi. Adaclip: Adapting clip with hybrid learnable prompts for zero-shot anomaly detection. In *European Conference on Computer Vision*, pages 55–72. Springer, 2025. 1, 2, 3, 6
- [9] Xuhai Chen, Yue Han, and Jiangning Zhang. A zero-/few-shot anomaly classification and segmentation method for cvpr 2023 vand workshop challenge tracks 1&2: 1st place on zero-shot ad and 4th place on few-shot ad. *arXiv preprint arXiv:2305.17382*, 2023. 2, 3, 6, 7
- [10] Xuhai Chen, Jiangning Zhang, Guanzhong Tian, Haoyang He, Wuhao Zhang, Yabiao Wang, Chengjie Wang, Yunsheng Wu, and Yong Liu. Clip-ad: A language-guided staged dual-path model for zero-shot anomaly detection. *arXiv preprint arXiv:2311.00453*, 2023. 2, 3, 6
- [11] Noel CF Codella, David Gutman, M Emre Celebi, Brian Helba, Michael A Marchetti, Stephen W Dusza, Aadi Kalloo, Konstantinos Liopyris, Nabin Mishra, Harald Kittler, et al. Skin lesion analysis toward melanoma detection: A challenge at the 2017 international symposium on biomedical imaging (isbi), hosted by the international skin imaging collaboration (isic). In *2018 IEEE 15th international symposium on biomedical imaging (ISBI 2018)*, pages 168–172. IEEE, 2018. 1, 6, 7
- [12] Deutsche Arbeitsgemeinschaft für Mustererkennung. Weakly supervised learning for industrial optical inspection, 2007. 6
- [13] Zhaopeng Gu, Bingke Zhu, Guibo Zhu, Yingying Chen, Hao Li, Ming Tang, and Jinqiao Wang. Filo: Zero-shot anomaly detection by fine-grained description and high-quality localization. In *Proceedings of the 32nd ACM International Conference on Multimedia*, pages 2041–2049, 2024. 2
- [14] Zixian Guo, Bowen Dong, Zhilong Ji, Jinfeng Bai, Yiwen Guo, and Wangmeng Zuo. Texts as images in prompt tuning for multi-label image recognition. In *Proceedings of the IEEE/CVF Conference on Computer Vision and Pattern Recognition*, pages 2808–2817, 2023. 2
- [15] Ziyu Guo, Renrui Zhang, Longtian Qiu, Xianzheng Ma, Xupeng Miao, Xuming He, and Bin Cui. Calip: Zero-shot enhancement of clip with parameter-free attention. In *Proceedings of the AAAI Conference on Artificial Intelligence*, pages 746–754, 2023. 2
- [16] A. Hamada. Br35h: Brain tumor detection 2020. *Online. Available: <https://www.kaggle.com/datasets/ahmedhamada0/brain-tumor-detection>*, 2020. 6
- [17] Steven A Hicks, Debesh Jha, Vajira Thambawita, Pål Halvorsen, Hugo L Hammer, and Michael A Riegler. The endotect 2020 challenge: evaluation and comparison of classification, segmentation and inference time for endoscopy. In *Pattern Recognition. ICPR International Workshops and Challenges: Virtual Event, January 10-15, 2021, Proceedings, Part VIII*, pages 263–274. Springer, 2021. 6
- [18] Jongheon Jeong, Yang Zou, Taewan Kim, Dongqing Zhang, Avinash Ravichandran, and Onkar Dabeer. Winclip: Zero-/few-shot anomaly classification and segmentation. In *Proceedings of the IEEE/CVF Conference on Computer Vision and Pattern Recognition*, pages 19606–19616, 2023. 1, 2, 3, 6
- [19] Debesh Jha, Pia H Smedsrud, Michael A Riegler, Pål Halvorsen, Thomas De Lange, Dag Johansen, and Håvard D Johansen. Kvasir-seg: A segmented polyp dataset. In *MultiMedia modeling: 26th international conference, MMM 2020, Daejeon, South Korea, January 5–8, 2020, proceedings, part II 26*, pages 451–462. Springer, 2020. 6, 7
- [20] Chao Jia, Yinfei Yang, Ye Xia, Yi-Ting Chen, Zarana Parekh, Hieu Pham, Quoc Le, Yun-Hsuan Sung, Zhen Li, and Tom Duerig. Scaling up visual and vision-language representation learning with noisy text supervision. In *International*

- conference on machine learning*, pages 4904–4916. PMLR, 2021. 1
- [21] Michael I Jordan, Zoubin Ghahramani, Tommi S Jaakkola, and Lawrence K Saul. An introduction to variational methods for graphical models. *Machine learning*, 37:183–233, 1999. 4
- [22] Pranita Balaji Kanade and PP Gumaste. Brain tumor detection using mri images. *Brain*, 3(2):146–150, 2015. 6
- [23] Diederik P Kingma. Auto-encoding variational bayes. *arXiv preprint arXiv:1312.6114*, 2013. 5
- [24] Diederik P Kingma and Jimmy Ba. Adam: A method for stochastic optimization. *arXiv preprint arXiv:1412.6980*, 2014. 6
- [25] Alexander Kirillov, Eric Mintun, Nikhila Ravi, Hanzi Mao, Chloe Rolland, Laura Gustafson, Tete Xiao, Spencer Whitehead, Alexander C Berg, Wan-Yen Lo, et al. Segment anything. In *Proceedings of the IEEE/CVF International Conference on Computer Vision*, pages 4015–4026, 2023. 2
- [26] Boyi Li, Kilian Q Weinberger, Serge Belongie, Vladlen Koltun, and Rene Ranftl. Language-driven semantic segmentation. In *International Conference on Learning Representations*, 2022. 2
- [27] Shengze Li, Jianjian Cao, Peng Ye, Yuhan Ding, Chongjun Tu, and Tao Chen. Clipsam: Clip and sam collaboration for zero-shot anomaly segmentation. *arXiv preprint arXiv:2401.12665*, 2024. 2
- [28] Shilong Liu, Zhaoyang Zeng, Tianhe Ren, Feng Li, Hao Zhang, Jie Yang, Qing Jiang, Chunyuan Li, Jianwei Yang, Hang Su, et al. Grounding dino: Marrying dino with grounded pre-training for open-set object detection. *arXiv preprint arXiv:2303.05499*, 2023. 2
- [29] Dwarikanath Mahapatra, Behzad Bozorgtabar, and Zongyuan Ge. Medical image classification using generalized zero shot learning. In *Proceedings of the IEEE/CVF international conference on computer vision*, pages 3344–3353, 2021. 1
- [30] Fausto Milletari, Nassir Navab, and Seyed-Ahmad Ahmadi. V-net: Fully convolutional neural networks for volumetric medical image segmentation. In *2016 fourth international conference on 3D vision (3DV)*, pages 565–571. Ieee, 2016. 5
- [31] Pankaj Mishra, Riccardo Verk, Daniele Fornasier, Claudio Piciarelli, and Gian Luca Foresti. Vt-adl: A vision transformer network for image anomaly detection and localization. In *2021 IEEE 30th International Symposium on Industrial Electronics (ISIE)*, pages 01–06. IEEE, 2021. 6
- [32] Zhen Qu, Xian Tao, Fei Shen, Zhengtao Zhang, and Tao Li. Investigating shift equivalence of convolutional neural networks in industrial defect segmentation. *IEEE Transactions on Instrumentation and Measurement*, 72:1–17, 2023. 1
- [33] Zhen Qu, Xian Tao, Mukesh Prasad, Fei Shen, Zhengtao Zhang, Xinyi Gong, and Guiguang Ding. Vcp-clip: A visual context prompting model for zero-shot anomaly segmentation. In *European Conference on Computer Vision*, pages 301–317. Springer, 2024. 2, 3, 6
- [34] Alec Radford, Jong Wook Kim, Chris Hallacy, Aditya Ramesh, Gabriel Goh, Sandhini Agarwal, Girish Sastry, Amanda Aspell, Pamela Mishkin, Jack Clark, et al. Learning transferable visual models from natural language supervision. In *International conference on machine learning*, pages 8748–8763. PMLR, 2021. 1, 2, 6
- [35] Yongming Rao, Wenliang Zhao, Guangyi Chen, Yansong Tang, Zheng Zhu, Guan Huang, Jie Zhou, and Jiwen Lu. Denseclip: Language-guided dense prediction with context-aware prompting. In *Proceedings of the IEEE/CVF conference on computer vision and pattern recognition*, pages 18082–18091, 2022. 2
- [36] Danilo Rezende and Shakir Mohamed. Variational inference with normalizing flows. In *International conference on machine learning*, pages 1530–1538. PMLR, 2015. 4
- [37] T-YLPG Ross and GKHP Dollár. Focal loss for dense object detection. In *proceedings of the IEEE conference on computer vision and pattern recognition*, pages 2980–2988, 2017. 5
- [38] David E Rumelhart, Geoffrey E Hinton, and Ronald J Williams. Learning representations by back-propagating errors. *nature*, 323(6088):533–536, 1986. 4
- [39] Mohammadreza Salehi, Niousha Sadjadi, Soroosh Baselizadeh, Mohammad H Rohban, and Hamid R Rabiee. Multiresolution knowledge distillation for anomaly detection. In *Proceedings of the IEEE/CVF conference on computer vision and pattern recognition*, pages 14902–14912, 2021. 6
- [40] Nima Tajbakhsh, Suryakanth R Gurudu, and Jianming Liang. Automated polyp detection in colonoscopy videos using shape and context information. *IEEE transactions on medical imaging*, 35(2):630–644, 2015. 6
- [41] Xian Tao, Xinyi Gong, Xin Zhang, Shaohua Yan, and Chandranath Adak. Deep learning for unsupervised anomaly localization in industrial images: A survey. *IEEE Transactions on Instrumentation and Measurement*, 71:1–21, 2022. 1
- [42] Ao Wang, Hui Chen, Lihao Liu, Kai CHEN, Zijia Lin, Jungong Han, and Guiguang Ding. YOLOv10: Real-time end-to-end object detection. In *The Thirty-eighth Annual Conference on Neural Information Processing Systems*, 2024. 1
- [43] Jiarui Xu, Shalini De Mello, Sifei Liu, Wonmin Byeon, Thomas Breuel, Jan Kautz, and Xiaolong Wang. Groupvit: Semantic segmentation emerges from text supervision. In *Proceedings of the IEEE/CVF Conference on Computer Vision and Pattern Recognition*, pages 18134–18144, 2022. 2
- [44] Hantao Yao, Rui Zhang, and Changsheng Xu. Visual-language prompt tuning with knowledge-guided context optimization. In *Proceedings of the IEEE/CVF conference on computer vision and pattern recognition*, pages 6757–6767, 2023. 2
- [45] Gunwoo Yong, Kahyun Jeon, Daeyoung Gil, and Ghang Lee. Prompt engineering for zero-shot and few-shot defect detection and classification using a visual-language pretrained model. *Computer-Aided Civil and Infrastructure Engineering*, 38(11):1536–1554, 2023. 2
- [46] Haomin Yu, Qingyong Li, Yunqiang Tan, Jinrui Gan, Jianzhu Wang, Yangli-ao Geng, and Lei Jia. A coarse-to-fine model for rail surface defect detection. *IEEE Transactions on Instrumentation and Measurement*, 68(3):656–666, 2018. 6

- [47] Kaiyang Zhou, Jingkang Yang, Chen Change Loy, and Ziwei Liu. Conditional prompt learning for vision-language models. In *Proceedings of the IEEE/CVF Conference on Computer Vision and Pattern Recognition*, pages 16816–16825, 2022. [2](#)
- [48] Kaiyang Zhou, Jingkang Yang, Chen Change Loy, and Ziwei Liu. Learning to prompt for vision-language models. *International Journal of Computer Vision*, 130(9):2337–2348, 2022. [2](#)
- [49] Qihang Zhou, Guansong Pang, Yu Tian, Shibo He, and Jiming Chen. Anomalyclip: Object-agnostic prompt learning for zero-shot anomaly detection. In *The Twelfth International Conference on Learning Representations*, 2023. [2](#), [3](#), [6](#), [7](#)
- [50] Yang Zou, Jongheon Jeong, Latha Pemula, Dongqing Zhang, and Onkar Dabeer. Spot-the-difference self-supervised pre-training for anomaly detection and segmentation. In *European Conference on Computer Vision*, pages 392–408. Springer, 2022. [6](#), [7](#)